Int. J. Electrochem. Sci., 13 **(2018)** 8006 – 8021, doi: 10.20964/2018.08.07

International Journal of
ELECTROCHEMICAL
SCIENCE
www.electrochemsci.org

An Efficient Carbon Coating Process Applied in Different Synthetic Routes of $LiFePO_4$ Cathode Materials

Guan Wu, Tingting Jiang, Xiaohui Tian, Yanbin Zhu, Yingke Zhou[*]

The State Key Laboratory of Refractories and Metallurgy, Institute of Advanced Materials and Nanotechnology, College of Materials and Metallurgy, Wuhan University of Science and Technology, Wuhan 430081, China
[*]E-mail: Zhouyingke@wust.edu.cn

Received: 22 March 2018 / *Accepted:* 20 May 2018 / *Published:* 5 July 2018

Four $LiFePO_4$/C composites have been successfully synthesized via Fe_2O_3 route, FeC_2O_4 route, $FePO_4$ route in solid-state method and $FeSO_4$ route in hydrothermal method with an efficient carbon coating process which innovatively employed compound carbon sources that consisted of fructose and calcium lignosulfonate. Kilogram grade pilot samples have been prepared and 2000 mAh pouch cells have been assembled and investigated. Due to the introduction of fructose and calcium lignosulfonate, the as-prepared $LiFePO_4$/C composites possess a layer of conductive carbon that contains calcium compound on the surface of $LiFePO_4$ particles, which are supposed to improve the electronic conductivity and reduce the side reaction between $LiFePO_4$ and electrolytes. All of the as-prepared $LiFePO_4$/C composites show different characteristics in full cells, the capacity retention of Fe_2O_3 derived LFP-S1 was as high as 92.2% after 400 days storage, the capacity retention of FeC_2O_4 derived LFP-S2 at 5C rate was 93.0%, the capacity retention of $FePO_4$ derived LFP-S3 at -20 ℃ was 66.7%, the capacity retention of $FeSO_4$ derived LFP-S4 was as high as 90.2% after 3000 cycles at 25 ℃.

Keywords: $LiFePO_4$; carbon coating; solid-state; Hydrothermal; Lithium-ion batteries

1. INTRODUCTION

Lithium-ion batteries are now widespread in electric devices, electric vehicles (EV) and energy storage system (ESS) [1-3]. Since the performances of lithium-ion batteries are mainly depended on the cathode materials, choose a proper cathode material is quite critical for lithium-ion batteries to achieve durable service life, high energy density and power density. Considerable efforts have been made to develop cathode materials with desirable properties such as improved performance, low cost and high safety [4]. So far, commercialized cathode materials of lithium-ion batteries mainly include

$LiFePO_4$, $LiMn_2O_4$ and $LiNi_xCo_yMn_{1-x-y}O_2$ materials. For $LiMn_2O_4$ cathode materials, due to the "Jahn-Teller" effect of Mn^{3+} lead to serious dissolution of Mn element, $LiMn_2O_4$ cathode suffers from poor cycling performance at high temperature [5]. For $LiNi_xCo_yMn_{1-x-y}O_2$ cathode materials, the layered structure was unstable, which directly resulted in poor thermal stability and safety problems of $LiNi_xCo_yMn_{1-x-y}O_2$ materials [6]. On the other hand, $LiFePO_4$ cathode presents many advantages such as the relatively high theoretical capacity (170 mAh g^{-1}), proper charge-discharge potential (~3.4 V versus Li^+/Li), low cost, environmental-friendly, excellent cycle life and structural stability [7]. The olivine structured lithium iron phosphate ($LiFePO_4$) has been widely researched since reported as a promising cathode material for lithium-ion batteries by Padhi et al. in 1997 [8]. Nevertheless, the intrinsic low lithium-ion diffusion and electronic conductivity directly lead to the poor rate capability and capacity loss, which are bottlenecks for the wide application of $LiFePO_4$ cathode [9,10].

Many efforts have been made to overcome the electronic and ionic transport limitations of $LiFePO_4$, including optimizing the size and morphology, doping with alien atoms, and coating with conductive carbon materials [5,11-13]. Among these strategies, the carbon coating is one of the most conventional methods to promote the specific capacity and rate performance by offering more routes for electron transfer and accelerating the transport of lithium ion. An efficient carbon coating technology plays an essential role in the manufacturing process of commercialized $LiFePO_4$ materials [14,15]. Various methods, such as solid-state reaction, hydrothermal/solvothermal synthesis, co-precipitation, sol-gel processing, microwave assisted synthesis, and spray pyrolysis, have been applied to synthesize the $LiFePO_4$/C composites [16-18]. The solid-state method is the most common technique to synthesize $LiFePO_4$/C materials in industrial production since it is facile to operate and easy for magnification. Fe_2O_3, FeC_2O_4 and $FePO_4$ are the main raw materials to provide the Fe source in the industrial solid-state production, and $LiFePO_4$/C products derived from different routes usually present different characteristics [19-23]. Besides, the hydrothermal method is also employed in industrial production due to it can make the morphology and particle size of $LiFePO_4$ controllable, $FeSO_4$ is commonly used as the raw material and the $LiFePO_4$/C products with controllable morphology and outstanding performances are usually obtained [24-27].

In this work, a mixture of carbon sources consisting of fructose and calcium lignosulfonate has been employed to form the carbon coating layer on the surface of $LiFePO_4$ particles, by using the solid-state method with respectively Fe_2O_3, FeC_2O_4, and $FePO_4$ as the Fe source, and hydrothermal method with $FeSO_4$ as the Fe source. Various characterizations and electrochemical tests have been carried out to investigate the impacts of different synthetic routes on the carbon coating process and the corresponding performances. Kilogram grade pilot samples have been prepared and 2000 mAh pouch cells have been assembled and investigated. The rate performances, low temperature performances, long term cycle performances and storage performances of the samples have been systematically tested. Due to the introduction of fructose and calcium lignosulfonate, the as-prepared $LiFePO_4$/C composites possess a coating layer of conductive calcium doped carbon, which are supposed to improve the electronic conductivity and reduce the side reaction between $LiFePO_4$ and electrolytes. Four as-prepared $LiFePO_4$/C composites show different characteristics. Among different synthetic routes of solid-state method, the sample derived from Fe_2O_3 route shows better storage performance, the sample derived from FeC_2O_4 route exhibits higher rate capability, and the sample

derived from $FePO_4$ route displays greatly improved cycle performance and higher capacity retention at low temperature. The $LiFePO_4$/C materials derived from the hydrothermal $FeSO_4$ route display excellent overall electrochemical performances and thermal stability. Form these characteristics of the obtained samples, the raw materials and synthesis routes can be selected to prepare suitable $LiFePO_4$/C composite materials with featured performances and suitable for different terminal applications.

2. EXPERIMENTAL

2.1 Preparation of materials

The $LiFePO_4$/C composites were prepared by the Fe_2O_3 route, FeC_2O_4 route, $FePO_4$ route with solid-state method and the $FeSO_4$ route with hydrothermal method, respectively. The synthesis procedures of Fe_2O_3 route were described as follows. Fe_2O_3 (≥ 99.5 wt%), Li_2CO_3 (≥99.5 wt%), LiH_2PO_4 (≥ 99.0 wt%), fructose (≥ 99.5 wt%), and calcium lignosulfonate (≥ 97.0 wt%) were used as starting materials, and the molar ratio of Li:Fe:P was controlled to be 1.03 : 0.97 : 1. The Fe_2O_3, LiH_2PO_4 and a small amount of fructose were successively added into a bead mill machine and ethanol was used as the solvent. Li_2CO_3 was added to adjust the Li content. After grinding, the fluidic mixture was dried by a spray drying process, annealed at 790 ℃ for 6 h in N_2 atmosphere and pulverized through a jet milling process. After that, the intermediate product was mixed with the rest of fructose and calcium lignosulfonate in the same bead mill machine to achieve adequate grinding, and then spray dried, annealed at 750℃ for 8 h in N_2 atmosphere, and jet milled to obtain the final $LiFePO_4$/C composites. The sample was named LFP-S1 in the following description.

The sample derived from FeC_2O_4 route was prepared as follows. FeC_2O_4 (≥ 99.5 wt%), Li_2CO_3 (≥ 99.5 wt%), $NH_4H_2PO_4$ (≥ 99.5 wt%), fructose (≥ 99.5 wt%), and calcium lignosulfonate (≥ 97.0 wt%) were used as raw materials, and the molar ratio of Li:Fe:P was controlled to be 1.03 : 0.97 : 1. The FeC_2O_4, Li_2CO_3, $NH_4H_2PO_4$ and a small amount of fructose were added into a bead mill machine in sequence, and ethanol was used as the solvent. After grinding, the fluidic mixture was dried by a spray drying process, annealed at 680 ℃ for 4 h in N_2 atmosphere and pulverized through a jet milling process. After that, the intermediate product was mixed with the rest of fructose and calcium lignosulfonate in the same bead milling machine to achieve adequate grinding, then spray dried, annealed at 720 ℃ for 8 h in N_2 atmosphere, and jet milled again to obtain the final $LiFePO_4$/C composites. The sample was named LFP-S2 in the following descriptions.

The sample derived from $FePO_4$ route was prepared as follows. $FePO_4$ (≥99.5 wt%), Li_2CO_3 (≥ 99.5 wt%), fructose (≥ 99.5 wt%), and calcium lignosulfonate (≥ 97.0 wt%) were used as raw materials, the molar ratio of Fe:P in the $FePO_4$ raw material was 0.97: 1, and the molar ratio of Li:Fe:P was controlled to be 1.03 : 0.97 : 1. The $FePO_4$, Li_2CO_3, fructose and calcium lignosulfonate were added into a bead mill machine in sequence, and deionized water was used as solvent. After adequate grinding, a well-distributed fluidic mixture was obtained, which was then dried by a spray drying process. After annealing at 720 ℃ for 10 h in N_2 atmosphere and pulverizing through a jet milling

process the $LiFePO_4$/C materials were obtained. The sample was named LFP-S3 in the following descriptions.

For the hydrothermal method, the sample was synthesized as follows. $LiOH \cdot H_2O$ (> 99.5 wt%), $FeSO_4 \cdot 7H_2O$ (> 99.5 wt%), H_3PO_4 (85 wt%) were used as raw materials, deionized water was used as the solvent. The LiOH solution and H_3PO_4 were firstly added into an autoclave under stirring to obtain a white suspension, and then the $FeSO_4$ solution and a proper amount of ascorbic acid were added. The molar ratio of Li:Fe:P was controlled to be 2.7: 0.97: 1 in the precursor solution. After that, the autoclave was sealed and heated to 180 ℃ and maintained for 6 h, then the obtained precipitates were washed with deionized water for several times. Then the precipitates were added into a solution with fructose and calcium lignosulfonate with stirring to form a well-distributed suspension, which was then dried by spray drying, annealed at 700 ℃ for 6 h in N_2 atmosphere and pulverized through a jet milling process to obtain the $LiFePO_4$/C composites. The sample was named LFP-S4 in the following descriptions.

2.2 Characterization

The crystal structures of all samples were identified by X-ray diffraction (XRD) using a Bruker D8 X-ray diffractometer with Cu K_α radiation, and the experimental diffraction patterns were collected by step scanning in the range of $15\ ^\circ \leq 2\theta \leq 85\ ^\circ$. Fourier transform infrared spectra (FTIR) of the materials were recorded from 4000 to 400 cm^{-1} by a Frontier FTIR spectrometer using the KBr pellet method. The particle distribution was confirmed by the Malvern Master Size 2000 analyzer. The Brunauer-Emmett-Teller (BET) method was performed to calculate the specific surface area using a TriStarII3020 analyzer. The carbon content was confirmed by a HCS-140 high frequency infrared carbon and sulfur analyzer (Dekai, Shanghai). The morphology of the samples was investigated by the ZEISS Sigma-02-33 scanning electron microscopy (SEM). The fine structure of the samples was examined by field emission FEI F20 transmission electron microscopy (TEM). The thermal stability of the samples was tested by a Netzsch STA449F3-QMS403C analyzer using differential scanning calorimetry (DSC) method. The coin cells were charged to 3.8 V before the cathode powder was scraped off the electrode to react with electrolyte, and the examination was performed over the range from 50 to 450 ℃ with a heating rate of 10 ℃/min

2.3 Electrochemical measurements

Electrochemical performances of the samples were tested with coin shaped half cells. The metallic lithium film was used as the counter and reference electrode. The liquid electrolyte is a solution of 1 M $LiPF_6$ in ethylene carbonate (EC)-ethyl methyl carbonate (EMC)-diethyl carbonate (DEC) (3:3:4 *V:V*). Microporous polypropylene film (Celgard 2400) was used as the separator. 90 wt% cathode materials, 5 wt% conductive carbon Super P and 5 wt% polyvinylidene fluoride (PVDF) binder were thoroughly mixed in N-methyl pyrrolidinone (NMP) and then pasted onto aluminum foil (16 μm) to perform as the working electrode. The electrodes were assembled into CR2430 coin cells in

an Ar filled glove box. The charge and discharge tests were performed over the voltage range of 2.0-3.8 V using a Land BTS-5V-50mA computer-controlled battery test station. CV tests were conducted over the voltage range between 2.0 and 4.2 V using a Bio-Logic VMP3B electrochemical workstation at the scanning rate of 0.1 mV s^{-1}, and EIS measurements were performed over the frequency range between 1 MHz and 100 mHz by using a ZAHNER Im6ex electrochemical workstation with an applied perturbation signal of 5 mV.

For further analysis of the practical performance, the pouch shaped full cells of all samples with a 2000 mAh rated capacity were fabricated. Commercialized graphite was employed as the anode. 94 wt% cathode materials, 2 wt% conductive carbon Super P and 4 wt% polyvinylidene fluoride (PVDF) binder were thoroughly mixed in N-methyl pyrrolidinone (NMP) and then pasted onto aluminum foil (16 μm) to perform as the cathode. The rate performances were tested over the voltage range of 2.0-3.65 V by a Neware 5V30A battery test station. The capacity retention at 0.5 C and the cyclic performances at 1 C at different temperatures were performed on the same Neware 5V30A battery test station connected with thermostats. The storage performances at 25 and 60 ℃ with a state of charge (SOC) of 100% at 0.5 C were also performed on the Neware 5V30A battery test station connected with thermostats.

3. RESULTS AND DISCUSSION

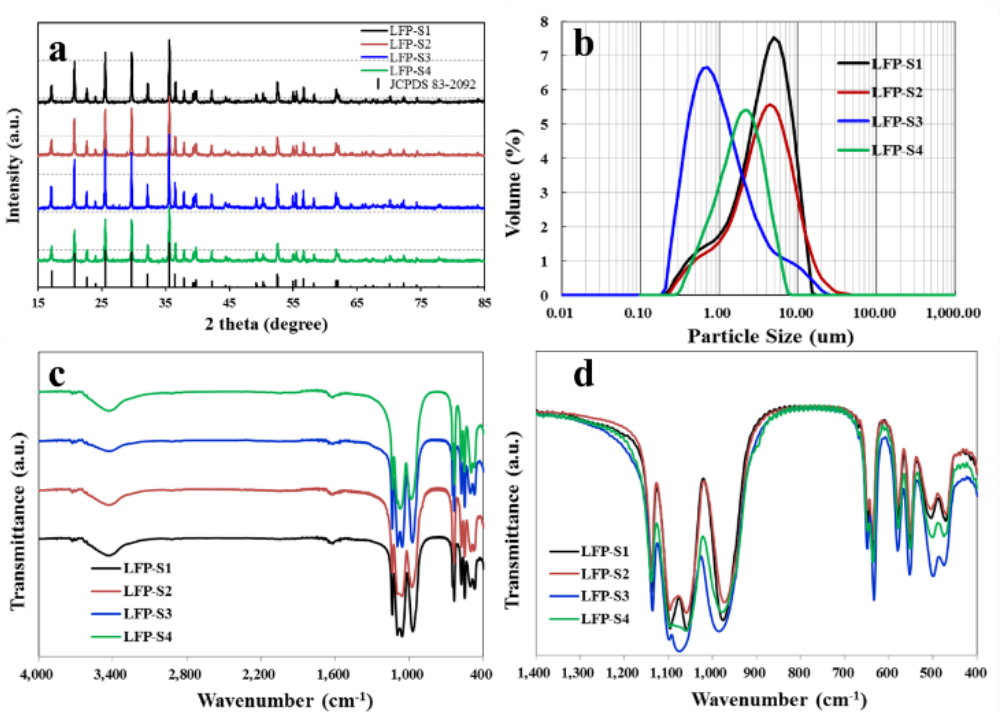

Figure 1. Physical characterizations of four LFP samples: (a) XRD patterns, (b) Particle size distribution curves, (c) FTIR spectra and (d) Comparison of the magnified FTIR spectra in the region of 400 and 1400 cm^{-1}.

Table 1. The particle size distribution parameters, specific surface area and carbon content of four LFP samples.

	Volume particle size (μm)				Specific surface area (m^2/g)	Carbon content (%)
	D10	D50	D90	D99		
LFP-S1	0.81	3.60	8.20	11.90	14.2	2.07
LFP-S2	0.83	3.58	9.50	20.10	16.7	1.85
LFP-S3	0.35	0.85	3.80	13.10	13.7	1.87
LFP-S4	0.68	1.81	3.92	5.91	15.6	1.91

The mixture of fructose and calcium lignosulfonate was used as carbon sources for the Fe_2O_3 route, FeC_2O_4 route, $FePO_4$ route in solid-state method and the $FeSO_4$ route in hydrothermal method, and finally the carbon coated composites of LFP-S1, LFP-S2, LFP-S3 and LFP-S4 were respectively obtained. All of the $LiFePO_4$/C composites were systematically characterized by various techniques. Fig.1a shows the XRD patterns of the as-synthesized composites. All peaks of the four patterns can be well indexed to an orthorhombic olivine-type phase (JCPDS No. 83-2092; space group: Pnma), and no peaks of impurities are found, indicating the high crystallinity and phase purity of all samples. Besides, there are also no characteristic lines of carbon and calcium compounds detected due to the low content. The peak intensity of LFP-S4 derived from the hydrothermal method is weaker than that of other samples, probably representing the smaller primary particles of LFP-S4 [12,28]. The particle size distribution curves are shown in Fig.1b and the results are displayed in Tab.1. The particle size distribution results indicating the second particles of all samples were well pulverized during the synthetic process, the D50 value of all four samples located at the range of 0.5~4 μm which guaranteed the high compact density during the electrode fabrication. The carbon contents of LFP-S1, LFP-S2, LFP-S3 and LFP-S4 are respectively 2.07%, 1.85%, 1.87% and 1.91%, indicating the same carbon coating level for all the samples. The specific surface areas of all samples were controlled at the range of 13~17 m^2/g to guarantee the process ability in the following cell producing process [29,30]. Fig.1c shows the FTIR spectra of all the as-synthesized materials in the region of 400-4000 cm^{-1}, and Fig.1d is the magnified region of 400-1400 cm^{-1} in Fig.1c. The stretching and bending vibrations of O-H are observed at around 3430 cm^{-1}, which can be attributed to the negligible amount of water and organic residue of carbon sources. The bands at about 1070, 980 and 630 cm^{-1} can be assigned to the C-O-C stretching vibrations, P-OH stretching vibrations, and C-OH bending vibrations, respectively. The mixture of fructose and calcium lignosulfonate was supposed to introduce considerable amount of active functional groups such as carboxyl and oxhydryl groups in all samples and result in improved electronic conductivity [22,31].

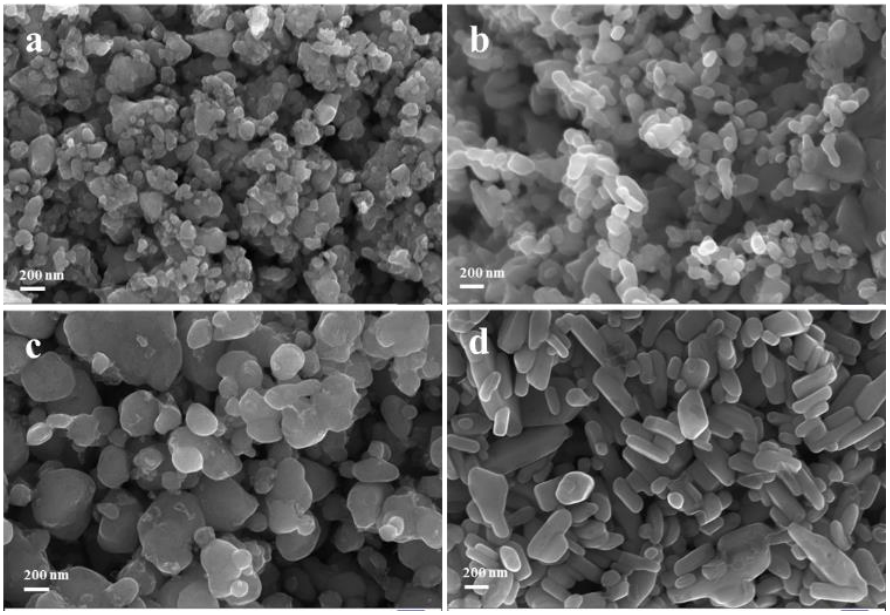

Figure 2. Typical SEM images: (a) LFP-S1, (b) LFP-S2, (c) LFP-S3, (d) LFP-S4.

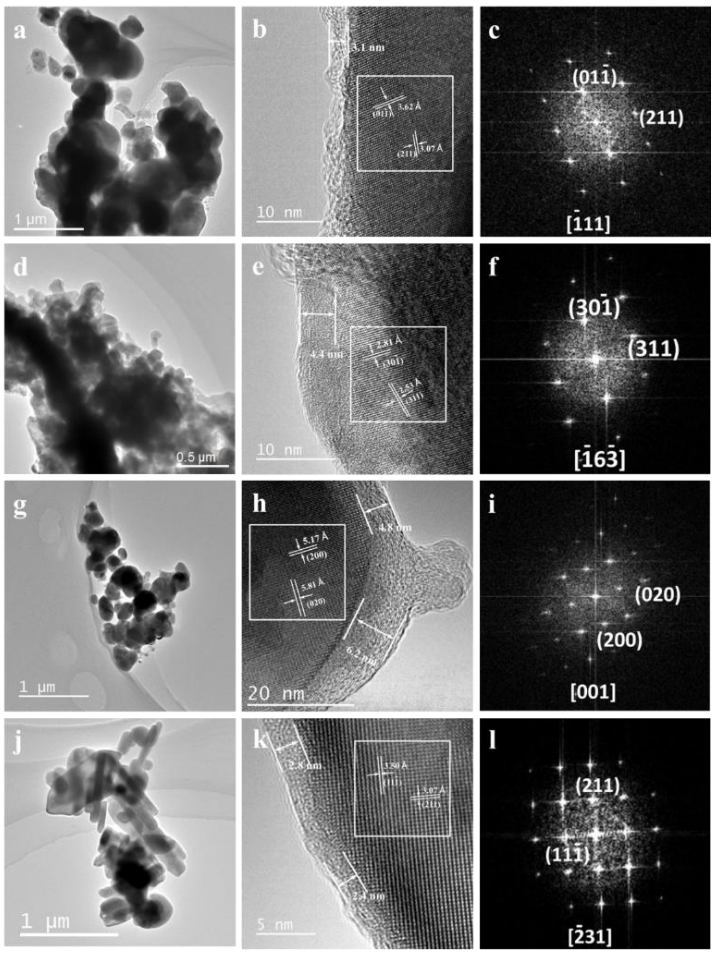

Figure 3. Typical TEM images: (a) LFP-S1, (d) LFP-S2, (g) LFP-S3, (j) LFP-S4; High-resolution TEM images: (b) LFP-S1, (e) LFP-S2, (h) LFP-S3, (k) LFP-S4; Electronic diffraction pattern in the corresponding marked zone: (c) LFP-S1, (f) LFP-S2, (i) LFP-S3, (l) LFP-S4.

Different peak intensities might be attributed to the different combination status between the residual organic functional groups and the carbon coating layer, which effected by the different superficial smoothness of $LiFePO_4$ particles. According to the principle of "like dissolves like", these residual active functional groups on the surface of $LiFePO_4$ particles are expected to improve the infiltration between cathode and electrolytes, which was supposed to accelerate the insertion/extraction reactions of lithium ions and enhance the electrochemical rate performances [32,33].

The typical SEM images of LFP-S1, LFP-S2, LFP-S3 and LFP-S4 are displayed in Fig.2a to Fig.2d, respectively. No redundant residual carbon can be found on the particle surface of all the samples, indicating the high efficiency of the carbon coating process with the introduction of the mixture of fructose and calcium lignosulfonate. For the Fe_2O_3 route derived LFP-S1 powder, the primary particle size is in the range of 100 to 500 nm, but aggregations clearly occur due to the high sintering temperature. For the LFP-S2 sample synthesized by the FeC_2O_4 route, the particles are more uniform and the primary particle size is mainly between 150 to 200 nm, the small and uniform particles usually corresponding to short average distance for the insertion/extraction process of lithium ions.

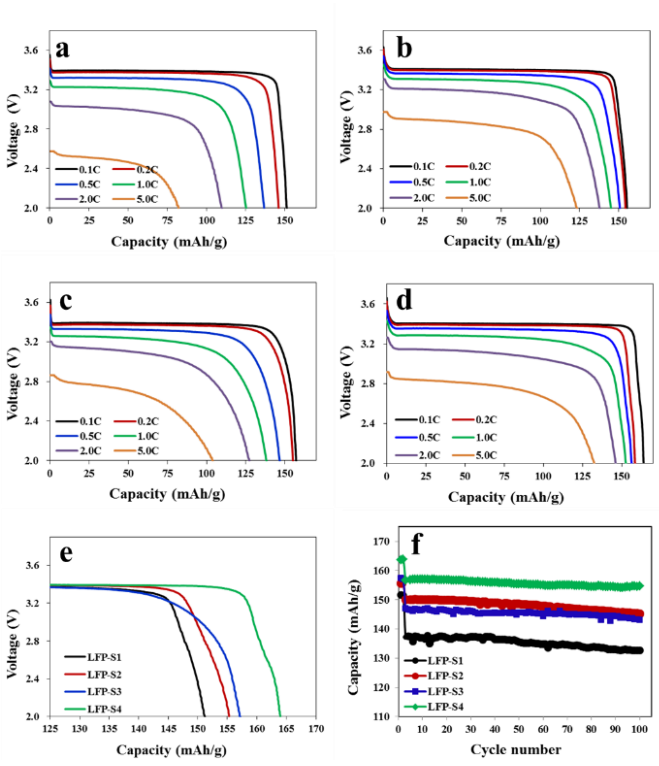

Figure 4. Discharge curves at different rates of (a) LFP-S1, (b) LFP-S2, (c) LFP-S3, (d) LFP-S4; (e) Comparison of the first discharge curves; (f) Comparison of cycling performances.

The primary particle size of LFP-S3 is about 200~400 nm, with a few large-sized particles. As $FePO_4$ is employed as the precursor, the morphology and particle size of LFP-S3 are easily affected by the applied $FePO_4$ raw material. For the LFP-S4 sample derived from the hydrothermal $FeSO_4$ route, the uniform rod-like primary particles with width of ~100 nm and length of 200~400 nm are observed. The smooth particle surfaces of all the four $LiFePO_4$ /C composites are attributed to the uniform

coating and tight integration between $LiFePO_4$ particles and the pyrolytic carbon from fructose and calcium lignosulfonate.

TEM measurements were performed to investigate the status of the carbon layer and the differences of crystal structure of the $LiFePO_4$ materials derived from different synthesis routes. Typical TEM images and the corresponding electron diffraction patterns of the samples are exhibited in Fig.3.

As shown in Fig.3a-c, small particles (~150 nm) and large particles (>500 nm) are simultaneously appeared in the LFP-S1 sample, the thickness of the carbon layer was about 2 nm to 4 nm. The (01-1) and (211) planes of olivine structures can be clearly identified along the [-111] axis in the corresponding electron diffraction pattern, which is consistent with the results of high resolution TEM image. TEM images of LFP-S2 are shown in Fig.3d-f, where the pyrolytic carbon layer with the thickness of ~4 nm is observed in the high resolution TEM image, and the (30-1) and (311) planes are found along the [-16-3] axis in the electron diffraction pattern. As shown in Fig.3g-i, the morphology of LFP-S3 is consistent with the SEM results, and clear lattice fringes are observed. The thickness of the coating carbon layer is about 4 to 6 nm, and the (020) and (200) planes of olivine structures are identified along the [001] zone axis. Typical TEM images and the corresponding electron diffraction pattern of LFP-S4 are shown in Fig.3j-l, where rod-like particles coated with a thin layer of carbon of ~3 nm are observed. Clear lattice fringes corresponding to the (11-1) and (211) planes are clearly observed along the [-231] axis in the high resolution image and confirmed in the electron diffraction patterns. The carbon layers of all the four samples are integrally coated on the surface of $LiFePO_4$ particles, indicating that the carbon coating processes employed here are highly efficient [34,35]. A small amount of calcium compounds was supposed to form on the surface of the $LiFePO_4$ particles as the calcium element introduced by calcium lignosulfonate, which may favor the surface stabilization. The differences of crystal structure of the four $LiFePO_4$/C composites derived from different synthesis routes are mainly ascribed to the different raw materials and synthesis conditions.

The electrochemical charge and discharge tests of the samples were performed over the voltage range of 2.0-3.8 V in coin cells. Shown in Fig.4a-d are the discharge curves of LFP-S1, LFP-S2, LFP-S3 and LFP-S4 at different rates from 0.1 C to 5 C. The discharge specific capacities of LFP-S1, LFP-S2, LFP-S3 and LFP-S4 are respectively 151.2, 155.3, 157.2 and 164.0 $mAhg^{-1}$ at 0.1 C, and are respectively 82.2, 123.5, 104.0 and 132.7 $mAhg^{-1}$ at 5 C. The LFP-S4 sample derived from the $FeSO_4$ route displays the highest specific capacity among the as-synthesized materials, probably ascribed to the excellent crystalline and uniform morphology with the hydrothermal method. Among the samples synthesized by the solid-state method, LFP-S3 derived from the $FePO_4$ route displays higher specific capacity than LFP-S1 and LFP-S2 at low rates of 0.1 and 0.2 C. However, at higher discharge rates, the LFP-S2 sample produced by the FeC_2O_4 route shows obvious advantages than LFP-S1 and LFP-S3. The higher specific capacity of LFP-S2 at high rates may result from the more uniform particles and smaller particle size with FeC_2O_4 in the solid-state synthesis. The magnified first discharge curves of all four samples at 0.1 C are exhibited in Fig.4e. The flat discharge potential plateau at around 3.4 V is similarly observed for all samples, but the ending parts of the discharge curves are quite different. The voltage plateau of LFP-S1 and LFP-S3 is lower than that of LFP-S2 and LFP-S4. Although the specific capacity of LFP-S3 is higher than that of LFP-S2, the slope of LFP-S3 at the end of the

discharge curve is much lower than that of LFP-S2, indicating the higher polarization of the LFP-S3 sample.

The charge/discharge tests were performed at 0.5 C for 100 times after activated the coin cells at 0.1 C for 2 cycles, and the cyclic curves of all the samples are shown in Fig.4f. After cycled for 100 times in coin cells, the capacity retention of LFP-S1, LFP-S2, LFP-S3 and LFP-S4 is 96.5%, 96.7%, 97.3% and 98.7%, respectively.

In order to confirm the thermal stability of the samples, the differential scanning calorimetry measurements (DSC) have been performed after charging the coin cells to 3.8 V. The DSC curves of LFP-S1, LFP-S2, LFP-S3 and LFP-S4 are respectively exhibited in Fig.5a-d. According to the DSC curves, the exothermic peaks and the corresponding areas can be respectively ascribed to the temperature of thermal runaway and the amount of released heat, which are originated from the reaction between the cathode and electrolyte [36]. The start temperatures of thermal runaway are 236.9, 252.3, 233.1 and 257.8 ℃ for LFP-S1, LFP-S2, LFP-S3 and LFP-S4, respectively. The total amounts of released heat of these four samples are 113.3, 117.9, 144.8 and 110.4 J/g, respectively. All the samples release a low amount of heat during the DSC tests, indicating the good thermal stability and high safety of the as-synthesized $LiFePO_4$/C composites with the carbon sources of fructose and calcium lignosulfonate. The overall thermal stability of LFP-S2 and LFP-S4 derived from the FeC_2O_4 route and $FeSO_4$ route are better than that of LFP-S1 and LFP-S3, probably attributed to the more uniform morphology and higher crystalline structure of LFP-S2 and LFP-S4.

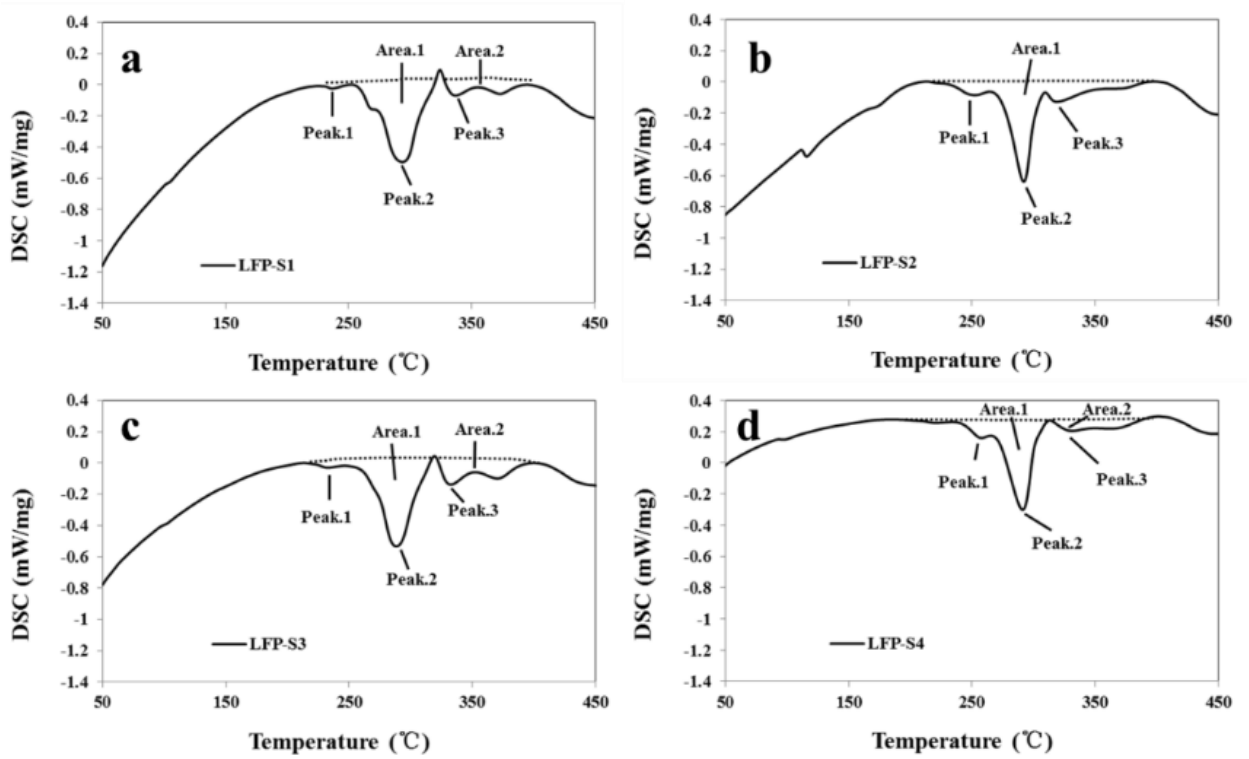

Figure 5. The DSC curves of (a) LFP-S1, (b) LFP-S2, (c) LFP-S3 and (d) LFP-S4.

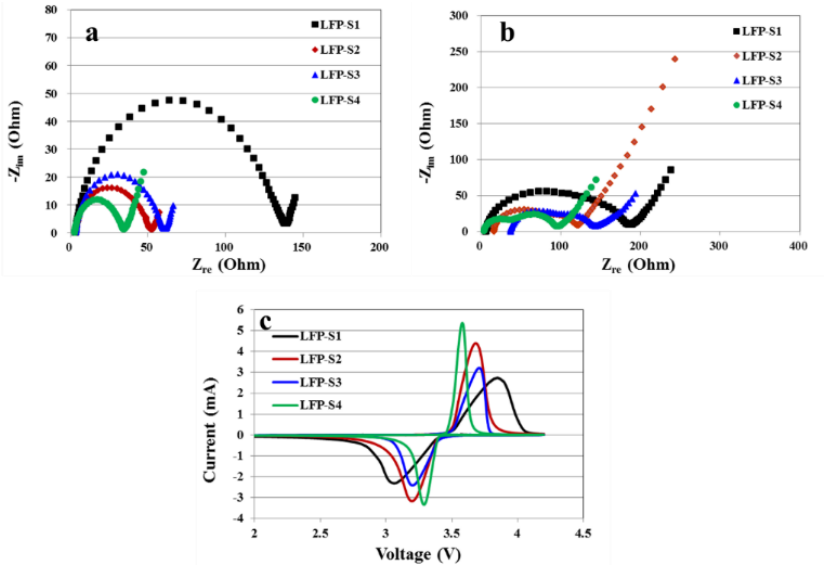

Figure 6. EIS curves of four samples: (a) 25 ℃, (b) 0 ℃; (c) Comparison of cyclic voltammetry results of four samples.

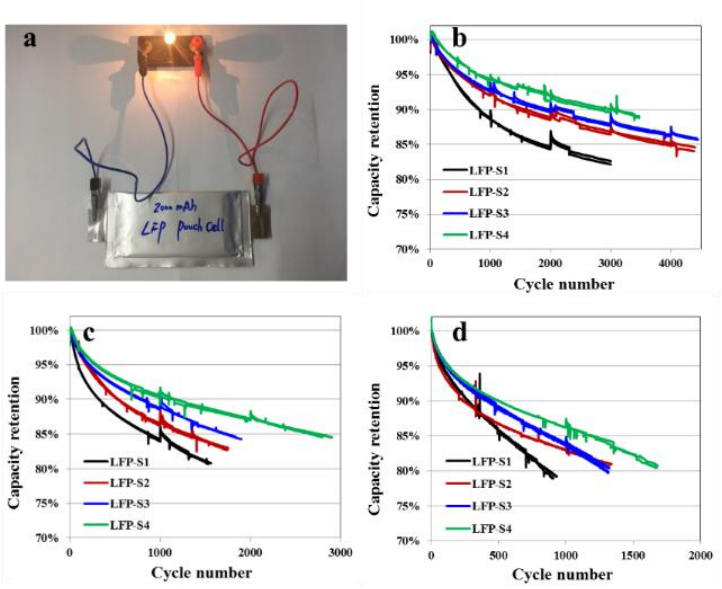

Figure 7. (a) Typical digital photo showing a lamp bulb is powered on with the LFP full cell; Comparison of the long-term cycling curves: (b) 25 ℃, (c) 45 ℃, (d) 60 ℃.

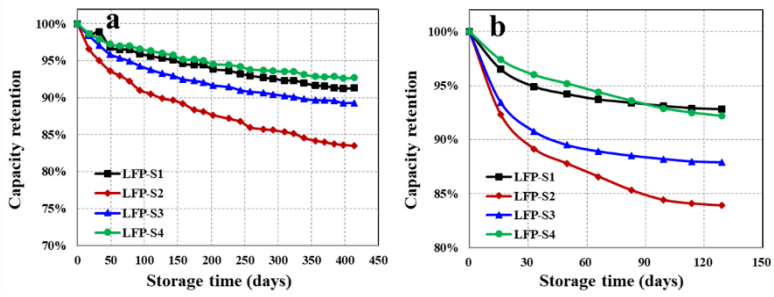

Figure 8. Long-term storage performances of the four samples: (a) 25 ℃, (b) 60 ℃.

The kinetic behaviors of the samples were further studied by EIS and CV measurements in coin cells. The EIS curves of all four samples at 25 and 0 ℃ are presented in Fig.6a and b, respectively. The charge transfer resistance of LFP-S1, LFP-S2, LFP-S3 and LFP-S4 at 25 ℃ is about 140, 50, 60 and 35 Ω, respectively. At low temperature, the LFP-S4 still displayed the lowest charge transfer resistance among four as-prepared samples, indicating the lowest polarization of LFP-S4. The cyclic voltammograms of the samples were measured over the voltage range of 2.0-4.2 V at the scan rate of 0.1 mV s^{-1}, as shown in Fig.6c. The LFP-S1 sample displays the broadest redox peaks among the four as-synthesized materials, which reveals obvious polarization of LFP-S1. The redox peaks of LFP-S2 are sharper than that of LFP-S3, and the voltage gap between the redox peaks of LFP-S4 is smaller than that of the other three samples. These results indicate that the LFP-S4 sample presents the highest kinetics, and LFP-S2 exhibits lower polarization than LFP-S3. Lower polarization is associated to higher reversibility and rate performances during the lithium insertion and extraction process [37,38].

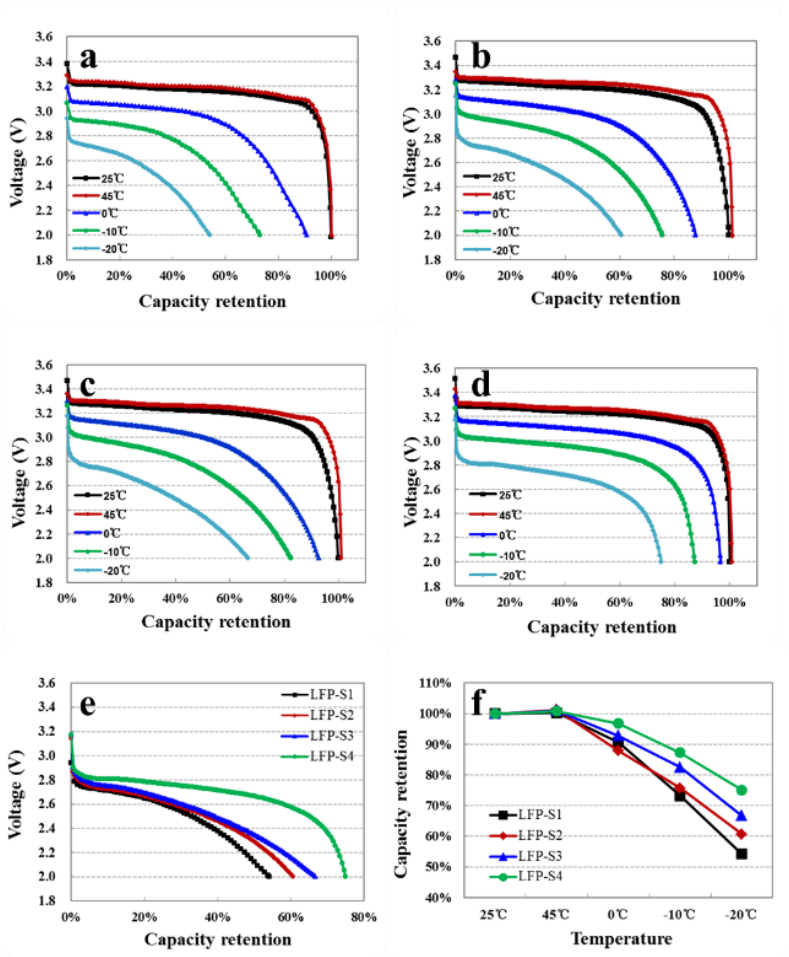

Figure 9. Discharge curves of the full cells at different temperatures: (a) LFP-S1, (b) LFP-S2, (c) LFP-S3, (d) LFP-S4; (e) Comparison of the discharge curves at -20 ℃; (f) Comparison of the capacity retention at different temperatures.

The scale-up synthesis of all four samples at kilogram-level were performed, and the pouch shaped full cells with a rated capacity of 2000 mAh were then fabricated to investigate the

electrochemical performances in practical application. Fig.7a displays a typical photo of a full cell powering a lamp bulb.

The long-term cycle tests of the full cells that respectively employed four as-prepared samples as cathode were conducted at the charge/discharge rate of 1 C. The results at different temperatures of 25, 45 and 60 ℃ are shown in Fig.7b-d respectively. Because of the efficient carbon coating process employed in this work, all four samples show acceptable cycle performances which can be utilized in various markets with different requirements. The LFP-S4 sample derived from the $FeSO_4$ route displays better cycle ability than that other three samples before the capacity retention fading to 80%, which is regarded as the failpoint of full cells in practical application. During the cycling at 25 and 45 ℃, the capacity retention of LFP-S2 derived from the FeC_2O_4 route is lower than that of LFP-S3 derived from the $FePO_4$ route. However, when cycling at 60 ℃, the capacity retention of LFP-S2 exceeds that of LFP-S3 after 1100 cycles, indicating the better durability of LFP-S2 at high temperature cycling, that may mainly because of the more uniform particles and smooth surfaces of LFP-S2 sample benefits the structural stability at high temperature.

The long-term storage performances of all four samples were tested after the cells were full charged, the storage curves at 25 and 60 ℃ are respectively displayed in Fig.8a and b. The LFP-S2 sample shows the lowest capacity retention during storage, which mainly ascribed to the highest specific surface area as which leads to more side effects between the particles and electrolyte, and accelerating the speed of capacity fading. The storage performance of LFP-S1 is slightly lower than that of LFP-S4 at 25 ℃. But after storage at 60 ℃ for about 100 days, the capacity retention of LFP-S1 exceeds that of LFP-S4. The advantage of LFP-S1 in high temperature storage is supposed to enlarge as the storage process continues. The featured durable storage performance of the LFP-S1 sample that derived from the Fe_2O_3 route is mainly because of the LFP-S1 material was originated from a higher calcination temperature that helps to break the Fe-O bond of Fe_2O_3 and finally achieved a more stable intrinsic crystalline structure.

The full cells of all $LiFePO_4$/C samples were tested at different temperatures to investigate the operational capability in different working conditions. The discharge curves of LFP-S1, LFP-S2, LFP-S3 and LFP-S4 at temperature of -20 to 45 ℃ are respectively displayed in Fig.9a-d. The discharge curves of the four samples at -20 ℃ are shown in Fig.9e to compare the discharge ability of the cells at low temperatures. Fig.9f is the overall comparison of the capacity retention of the four samples at different temperatures. The discharge voltage plateau of LFP-S1 is a little lower than that of the other samples, especially at 25 and 45 ℃, indicating the higher polarization brought by the Fe_2O_3 route. The capacity retention of LFP-S1, LFP-S2, LFP-S3 and LFP-S4 at -20 ℃ is 54.2%, 60.7%, 66.7% and 75.1%, respectively. The LFP-S4 sample shows the best discharge ability at low temperature, and the capacity retention of LFP-S3 at -10 and -20 ℃ is higher than that of LFP-S1 and LFP-S2. This may mainly due to the similar crystalline structure of $FePO_4$ and $LiFePO_4$ which resulted in the $FePO_4$ route benefits the process of Li^+ insertion and extraction at low temperatures.

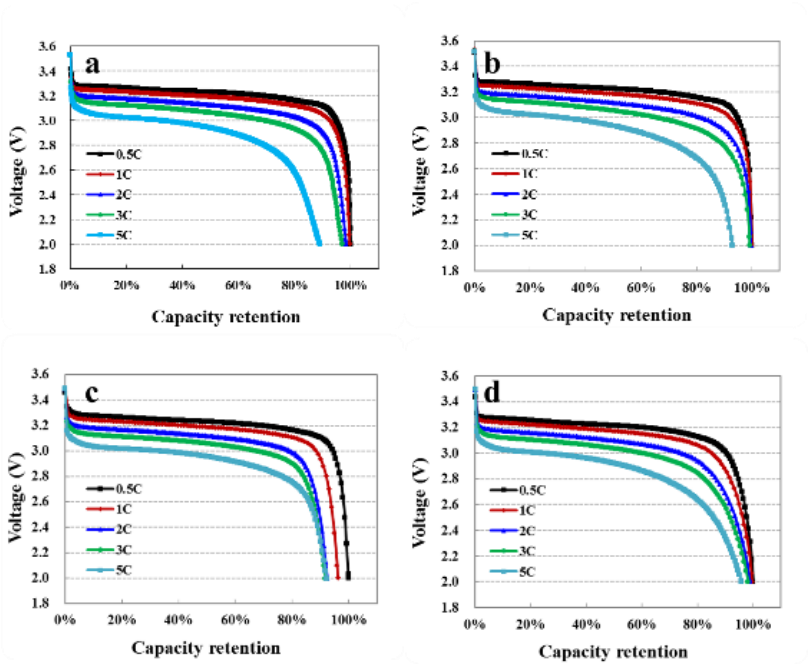

Figure 10. Discharge curves of the full cells at different rates: (a) LFP-S1, (b) LFP-S2, (c) LFP-S3, (d) LFP-S4.

The discharge curves of LFP-S1, LFP-S2, LFP-S3 and LFP-S4 at 0.5 to 5 C are respectively shown in Fig.10a-d to compare the rate performances. All four samples present rather high capacity retention at high discharge rates due to the high quality and conductivity of the carbon coating layer. The capacity retention of LFP-S1, LFP-S2, LFP-S3 and LFP-S4 is respectively 96.8%, 99.3%, 91.8% and 98.2% at 3 C, and respectively 88.9%, 93.0%, 92.2% and 95.9% at 5 C rate. The LFP-S2 sample from the FeC_2O_4 route displays the highest discharge capacity retention at 0.5 to 3 C, and the LFP-S4 sample from the $FeSO_4$ route shows the highest discharge capacity retention at 5 C. The better discharge ability of LFP-S2 and LFP-S4 at high rate is mainly attributed to the uniform morphology and nanoscale structure, which shorten the distance and accelerated the speed of Li^+ insertion/extraction process in $LiFePO_4$ particles.

As mentioned above, the solid-state reaction is the most facile method to obtain $LiFePO_4$ materials in mass production. The Fe_2O_3 route, FeC_2O_4 route and $FePO_4$ route are most commonly applied in the solid-state synthesis [5, 15-19]. For the LFP-S1 material obtained from the Fe_2O_3 route in this work, the prime cost is the lowest due to the cheapness of the Fe_2O_3 raw material. The LFP-S1 material displays acceptable overall electrochemical performances and outstanding storage performances, which is appropriate for utilizations in the market of energy storage system with strict requirements on the cost and long-term storage performances.

The LFP-S2 material synthesized by the FeC_2O_4 route is composed of nano-scaled particles and the prime cost is also relative low. In addition, the LFP-S2 material exhibits particularly excellent rate performances, which can be well supplied in the market of high power electric tools and devices that demand prominent discharge ability at high rates.

The LFP-S3 material displays remarkable processability, high specific capacity and reasonably well low temperature performances, and the corresponding $FePO_4$ route is facile for the high-volume production because of its simple one-step process and relatively low cost. Therefore, the LFP-S3 material is qualified for the market of electric buses where large quantity of active materials with stable production process are rigidly demanded.

Although the solution based synthesis is usually related to more complicated procedures and facilities and higher cost of production, it is more advantageous to control the crystal growth, morphology and particle size of $LiFePO_4$ materials [22,31]. The solution based hydrothermal method has been applied to the mass production of $LiFePO_4$ in recent years. The LFP-S4 material originated from the hydrothermal $FeSO_4$ route presents high specific capacity, high thermal stability and safety, and superiority long-term cycling performance and low temperature performance. Therefore, the $LiFePO_4$/C products synthesized by the $FeSO_4$ route in this work are suitable for applications in the high-end electric automobiles and devices that require high energy density and long service time but with high tolerance to cost.

4. CONCLUSIONS

Herein, $LiFePO_4$/C composites have been successfully synthesized by the solid-state Fe_2O_3 route, FeC_2O_4 route, $FePO_4$ route and the hydrothermal $FeSO_4$ route, with an efficient carbon coating process using the dual carbon sources of fructose and calcium lignosulfonate. All of the prepared $LiFePO_4$/C samples are coated by a thin layer of continuous carbon with high conductivity. The residual pyrolytic carbon layer contains a certain amount of organic functional groups introduced by the fructose and calcium lignosulfonate. These active functional groups assist to improve the reactivity of cathode and the infiltration between cathode and electrolytes. Besides, a small quantity of calcium compounds formed on the surface of $LiFePO_4$ particles which favor the surface stability and depress the side reaction between $LiFePO_4$ and electrolytes. Therefore, the efficient carbon coating technology introduced in this work enables the excellent overall electrochemical performances of all the as-synthesized $LiFePO_4$/C samples. Depending on the different procedures, the synthesized materials exhibit different features and can be promisingly applied as the potential cathode for lithium-ion batteries.

ACKNOWLEDGEMENTS
This work was supported by the National Natural Science Foundation of China (No. 51372178) and the Natural Science Foundation for Distinguished Young Scholars of Hubei Province of China (No. 2013CFA021).

References

1. Y.H. Huang, J.B. Goodenough, *Chem. Mater.*, 20 (2016) 7237.
2. M.S. Whittingham, *Chem. Rev.*, 104 (2004) 4271.
3. J.J. Wang, X.L. Sun, *Energy Environ. Sci.*, 8 (2015) 1110.

4. K.X. Wang, X.H. Li, J.S. Chen, *Adv. Mater.*, 27 (2015) 527.
5. D.K. Kim, P. Muralidharan, H.W. Lee, R. Ruffo, Y. Yang, C.K. Chan, H.L. Peng, R.A. Huggins, Y Cui, *Nano Lett.*, 8 (2008) 3948.
6. H. Kaneda, Y. Koshika, T. Nakamura, H. Nagata, R. Ushio, K. Mori, *Int. J. Electrochem. Sci.*, 12 (2017) 4640.
7. H.C. Kang, D.K. Jun, B. Jin, E.M. Jin, K.H. Park, H.B. Gu, *J. Power Sources*, 179 (2008) 340.
8. A.K. Padhi, K.S. Nanjundaswamy, J.B. Goodenough, *J. Electrochem. Soc.*, 144 (1997) 1188.
9. J. Lu, Z.H. Chen, Z.F. Ma, F. Pan, L.A. Curtiss, K. Amine, *Nat. Nanotechnol.*, 11 (2016) 1031.
10. Y.K. Zhou, J. Wang, Y.Y. Hu, R. O'Hayre, Z.P. Shao, *Chem. Commun.* 46 (2010) 7151.
11. A.V. Murugan, T. Muraliganth, A. Manthiram, *J. Phys. Chem. C*, 112 (2008) 46.
12. G. Wu, R. Ran, B. Zhao, Y.J. Sha, C. Su, Y.K. Zhou, Z.P. Shao, *J. Energy Chem.*, 23 (2014) 363.
13. L.H. Hu, F.Y. Wu, C.T. Lin, A.N. Khlobystov, L.J. Li, *Nat. Commun.*, 4 (2013) 1687.
14. G. Wu, Y.K. Zhou, Z.P. Shao, *Appl. Surf. Sci.*, 283 (2013) 999.
15. R.R. Chen, Y.X. Wu, X.Y. Kong, *J. Power Sources*, 258 (2014) 246.
16. H. Kim, H. Kim, S.W. Kim, K.Y. Park, J. Kim, S. Jeon, K. Kang, *Carbon*, 50 (2012) 1966.
17. W. Wei, P. Qu, M.T. Xu, X.Y. Qiu, L.L. Guo, L. Guo, *Rsc Adv.*, 5 (2015) 37830.
18. K. Dokko, S. Koizumi, H. Nakano, K. Kanamura, *J. Mater. Chem.*, 17 (2007) 4803.
19. A. Yamada, S. C. Chung, K. Hinokuma, *J. Electrochem. Soc.*, 148 (2001) A224.
20. L. Laffont, C. Delacourt, P. Gibot, M.Y. Wu, P. Kooyman, C. Masquelier, *Chem. Mater.*, 18 (2014) 5520.
21. Z.H. Chen, J.R. Dahn, *J. Electrochem. Soc.*, 149 (2002) A1184.
22. X.L. Wu, L.Y. Jiang, F.F. Cao, Y.G. Guo, L.J. Wan, *Adv. Mater.*, 21 (2009) 2710.
23. P.P. Prosini, D. Zane, M. Pasquali, *Electrochim. Acta*, 46 (2001) 3517.
24. S.S. Zhang, J.L. Allen, K.Xu, T.R. Jow, *J. Power Sources*, 147 (2005) 234.
25. K. Dokko, S. Koizumi, K. Sharaishi, K. Kanamura, *J. Power Sources*, 165 (2007) 656.
26. G. Meligrana, C. Gerbaldi, A. Tuel, S. Bodoardo, N. Penazzi, *J. Power Sources*, 160 (2006) 516.
27. J. Qian, M. Zhou, Y. Cao, X. Ai, H. Yang, *J. Phys. Chem. C*, 114 (2010) 3477.
28. K. Shiraishi, K. Dokko, K. Kanamura, *J. Power Sources*, 146 (2005) 555.
29. B. Jin, H.B. Gu, *Solid State Ionics*, 178 (2008) 1907.
30. B. Scrosati, J. Hassoun, Y.K. Sun, *Energy Environ. Sci.*, 4 (2011) 3287.
31. H. Liu, C. Li, H.P. Zhang, L.J. Fu, Y.P. Wu, H.Q. Wu, *J. Power Sources*, 159 (2006) 717.
32. Y.W. Chen, J.S. Chen, *Int. J. Electrochem. Sci.*, 7 (2012) 8128.
33. Z. Ma, G. Shao, G. Wang, J. Du, Z. Ying, *Ionics*, 19 (2013) 437.
34. A. Liu, Y. Liu, Z. Hu, G. Gao, Y. Xu, L. Lei, *J. Phys. Chem. Solids*, 72 (2011) 831.
35. S. Yoo, B. Kang, *J. Mater. Chem. A*, 3 (2015) 13906.
36. S.W. Zhu, M.X. Jing, Z.C. Pi, L.L. Chen, X.Q. Shen, *Int. J. Electrochem. Sci.*, 10 (2015) 10597.
37. Y. Koyama, T. Uyama, Y. Orikasa, T. Naka, H. Komatsu, K. Shimoda, H. Murayama, K. Fukuda, H. Arai, E. Matsubara, Y. Uchimoto, Z. Ogumi, *Chem. Mater.*, 29 (2017) 2855.
38. P.H. Xiao, G. Henkelman, *ACS Nano*, 12 (2018) 844.